RSC Advances

ROYAL SOCIETY OF CHEMISTRY

www.rsc.org/advances

Graphic abstract

A facile and novel anion-exchange strategy was developed for 3D hierarchical $(BiO)_2CO_3$/amorphous Bi_2S_3 heterostructures with highly enhanced visible light photocatalysis.

Na₂S

Anion Exchange

$BiO)_2CO_3$ + Na_2S ⟶ $(BiO)_2CO_3$/**amorphous Bi_2S_3 heterostructures**

RSC Advances
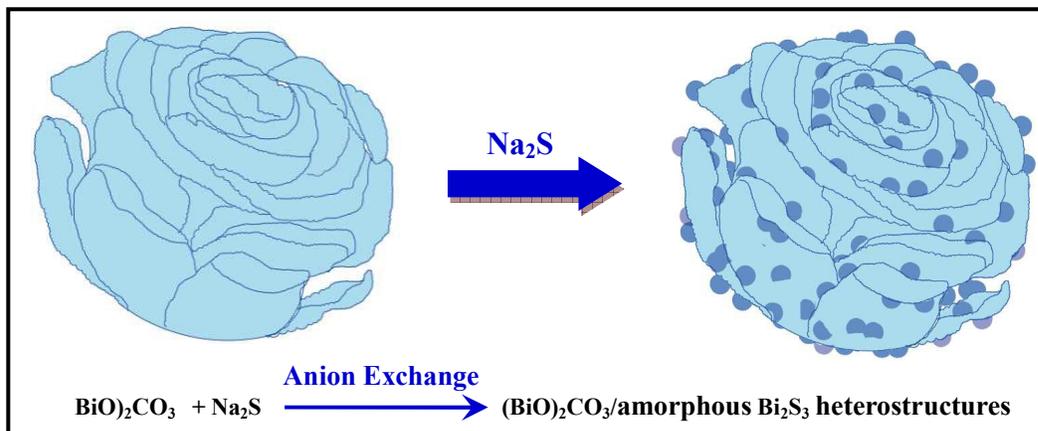
Full Paper

An anion-exchange strategy for 3D hierarchical (BiO)$_2$CO$_3$/amorphous Bi$_2$S$_3$ heterostructures with increased solar absorption and enhanced visible light photocatalysis

Fan Dong [a],*, Xin Feng [a], Yuxin Zhang [b], Chunfeng Gao [a], and Zhongbiao Wu [c],*

Abstract: Bismuth-based nanostructured materials have been attracted great interest in a wide range of applications. In the present work, 3D (BiO)$_2$CO$_3$ hierarchical microspheres self-assembled by nanosheets were synthesized by a
10 simple hydrothermal method. By using a facile anion-exchange strategy, (BiO)$_2$CO$_3$/amorphous Bi$_2$S$_3$ heterostructures were constructed through the controlled chemical reaction between (BiO)$_2$CO$_3$ microspheres and Na$_2$S in an aqueous solution. The as-prepared samples were systematically characterized by XRD, SEM-EDX, TEM, FT-IR, XPS, UV-vis DRS and PL techniques. The
15 heterostructured samples were applied for photocatalytic removal of ppb-level NO in air under visible light irradiation. The pure (BiO)$_2$CO$_3$ hierarchical microspheres exhibited decent visible light photocatalytic activity due to the surface reflecting and scattering effect. Amorphous Bi$_2$S$_3$ showed no photocatalytic activity due to narrow band gap. By hybridization of (BiO)$_2$CO$_3$ microspheres with amorphous
20 Bi$_2$S$_3$ on the surface, 3D hierarchical (BiO)$_2$CO$_3$/amorphous Bi$_2$S$_3$ heterostructures were constructed, which demonstrated increased solar light absorption and highly enhanced visible photocatalytic activity and stability. The enhanced performance can be directly ascribed to the increased visible light utilization, promoted charge separation arising from the well-matched band structure and accelerated reactants
25 transfer resulting from special 3D hierarchical structure. The present work opens a new avenue for modification of wide-band gap semiconductor with amorphous components, which could reduce the further thermal treatment and production cost.

1. Introduction

In recent years, bismuth-based nanostructured materials are receiving great attention due to their potential
30 applications in photocatalysts, semiconductor technology, thermal catalysts, energy conversion and electronics.[1-4] Especially, bismuth-based semiconductor nanohybrid with a staggered alignment of band edges at the heterointerface could greatly extend spectral responsive range of wide-band gap semiconductor and significantly reduce the recombination of the photogenerated electrons and holes, thus effectively improving the photocatalytic activity of single-component material.[5-9] Up to now, various kinds of Bi-based heterostructures have been
35 synthesized, such as BiOCl/Bi$_2$S$_3$,[10] BiVO$_4$/Bi$_2$S$_3$,[11] BiOI/Bi$_2$S$_3$,[12] (BiO)$_2$CO$_3$/BiOI,[13] BiOI/BiOCl,[14] Bi$_2$MoO$_6$/BiOCl [15] and so on.

Hierarchical bismuth-containing materials composed of 2D nanosheets or nanoplates have been developed and exhibited excellent visible light photocatalytic performance, such as Bi$_2$WO$_6$, Bi$_2$MoO$_6$, BiVO$_4$, BiOX (X=Br, I),

[a] Chongqing Key Laboratory of Catalysis and Functional Organic Molecules, College of Environmental and Biological Engineering, Chongqing Technology and Business University, Chongqing, 400067, China
[b] College of Materials Science and Engineering, Chongqing University, Chongqing, 400044, P.R. China.
[c] Department of Environmental Engineering, Zhejiang University, Hangzhou, Zhejiang 310027, China.
∗ To whom correspondence should be addressed.
E-mail: dfctbu@126.com (Fan Dong); zbwu@zju.edu.cn (Zhonbiao Wu). Tel.: +86-23-62769785-605; Fax: +86-23-62769785-605.

1

BiFeO$_3$, Bi$_2$Ti$_2$O$_7$, Bi$_2$Sn$_2$O$_7$ and (BiO)$_2$CO$_3$.[16-28] These 2D nanostructures can be acted as building blocks for construction of 3D architectures. 3D architectures favored the transfer of electrons and holes generated inside the crystal surface and promoted charge separation, which could enhance the photocatalytic activity.[14,28-30] Recently, (BiO)$_2$CO$_3$ is found to be an emergent attractive photocatalyst.[28-33] However, pure (BiO)$_2$CO$_3$ with large band gap (3.1-3.5 eV) can only be excited by UV light.[31-33] Thus, it is important to extend the light absorption spectra of (BiO)$_2$CO$_3$ into visible light region so that the modified (BiO)$_2$CO$_3$ could utilize the abundant solar light. Nitrogen doping,[29,30,33] silver decoration,[25,32] and formation of heterojunction[26,27,34] have been employed to achieve this goal.

(BiO)$_2$CO$_3$ has a typical layered structure with alternative stacking of (BiO)$_2^{2+}$ sheets interleaved by CO$_3^{2-}$ groups.[29-32] This special crystal structure could behave as an excellent host material for further modification. Firstly, we must find out a semiconductor that has a low solubility parameter and narrow band gap, which could combine with (BiO)$_2$CO$_3$ through anion change. The combination of two semiconductors with different energy levels could form an effective heterostructure with enhanced charge separation.[9,11,35-38] Fortunately, Bi$_2$S$_3$ is a such semiconductor that could fulfill the requirements. Bi$_2$S$_3$ is direct semiconductor with a narrow band gap (~1.3 eV). It has many applications such as thermoelectrics, photovoltaics, X-ray computed tomography, and electrochemical hydrogen storage.[39-42] The solubility constant (K$_{sp}$) of Bi$_2$S$_3$ (1×10^{-97}) is much lower than that of (BiO)$_2$CO$_3$ (3.98×10^{-36}). On the basis of the precipitation and dissolution equilibrium, product with higher solubility product constant (K$_{sp}$) will be converted into product with lower K$_{sp}$ in solution, which is also called ion exchange reaction. Although (BiO)$_2$CO$_3$/Bi$_2$S$_3$ has been reported, the Bi$_2$S$_3$ component on the surface of (BiO)$_2$CO$_3$ is well crystallized by hydrothermal treatment.[43-45]

In the present work, to promote the photocatalytic activity of (BiO)$_2$CO$_3$ under visible light irradiation, we developed an anion-exchange strategy for the construction of 3D hierarchical (BiO)$_2$CO$_3$/amorphous Bi$_2$S$_3$ heterostructures with increased solar absorption and enhanced visible light photocatalytic performance. The (BiO)$_2$CO$_3$/amorphous Bi$_2$S$_3$ heterostructures were constructed by a facile anion exchange reaction between (BiO)$_2$CO$_3$ and Na$_2$S. As the K$_{sp}$ of Bi$_2$S$_3$ is lower than that of (BiO)$_2$CO$_3$, part of (BiO)$_2$CO$_3$ could be converted into Bi$_2$S$_3$ easily in the presence of Na$_2$S. The content of Bi$_2$S$_3$ can be controlled by the amount of Na$_2$S. The photocatalytic activity of the obtained (BiO)$_2$CO$_3$/amorphous Bi$_2$S$_3$ heterostructures was evaluated for removal of NO at ppb-level under visible light. Significantly, the as-prepared heterostructured photocatalysts exhibited highly enhanced visible light activity and photochemical stability during photocatalytic removal of NO in air, which can be directly ascribed to the formation of heterostructures and special 3D hierarchical structure. The construction of heterostructures by amorphous Bi$_2$S$_3$ has significant advantages of facile synthesis and low cost. The present work could shed new light on the fabrication of high-performance heterostructured photocatalysts by modification with amorphous component.

2. Experimental Section

2.1 Synthesis of (BiO)$_2$CO$_3$ hierarchical microspheres.

All chemicals used in this study were analytical grade and were used without further purification. In a typical fabrication, sodium carbonate (0.46 g) were added with 70 ml distilled water into a 100 mL autoclave Teflon vessel and stirred for 10 min. Then bismuth citrate (1.60 g) was added to the solution and stirred for another 30 min. The resulted aqueous precursor suspension was then hydrothermally treated at 160 °C for 24 h. The obtained solid sample was filtered, washed with water and ethanol for three times, and dried at 60 °C to get final (BiO)$_2$CO$_3$ (hereinafter referred to BOC).

2.2 Construction of (BiO)$_2$CO$_3$/amorphous Bi$_2$S$_3$ heterostructures.

In a typical process, 0.75 g of (BiO)$_2$CO$_3$ was added into 60 mL distilled water, and then ultrasound dispersed for 30 min. The aqueous suspension was put into thermostat water bath at 60 °C and stirring. Then the 40 mL of Na$_2$S aqueous solution was added to the above solution under continuous stirring for another 2 h. The sample obtained was filtered, washed with water and ethanol for four times and dried at 60 °C to get the final products. The amount of Na$_2$S in the solution is controlled at 0.0175, 0.0350, 0.0875, 0.1750 and 0.3500 g, respectively. The molar ratio of Bi$_2$S$_3$ to (BiO)$_2$CO$_3$ is 0.05, 0.10, 0.25, 0.50 and 1.0, respectively. Accordingly, the resulted products were labeled as BS-0.05, BS-0.10, BS-0.25, BS-0.50 and BS-1.00, respectively.

2.3 Characterization methods

The crystal structure of the as-obtained sample were analyzed by X-ray diffraction with Cu-Karadiation (XRD: model D/max RA, Rigaku Co., Japan). The morphological structure were examined by transmission electron microscopy (TEM:JEM-2010, Japan). X-ray photoelectron spectroscopy with Al Kα X-rays (hν=1486.6 eV) radiation operated at 150W (XPS: Thermo ESCALAB 250,USA) was used to investigate the surface properties. The shift of the binding energy due to relative surface charging was corrected using the C1s level at 284.8 eV as an internal standard. The Brunauer–Emmett–Teller (BET) surface area and the pore size distribution of the products were identified by a Micromeritics ASAP 2020 apparatus. All the samples were degassed at 150 °C prior to

measurements. The UV-vis diffuse reflection spectra were obtained for the dry-pressed disk samples using a Scan UV-vis spectrophotometer (UV-vis DRS: UV-2450, China) equipped with an integrating sphere assembly, using 100% $BaSO_4$ as reflectance sample. FT-IR spectra were recorded on a Nicolet Nexus spectrometer on samples embedded in KBr pellets. The solid-state photoluminescence (PL) spectra were measured with fluorescence spectrophotometer (PL: FS-2500, Japan) using a Xe lamp as an excitation source with optical filters.

2.4 Evaluation of visible light photocatalytic performance

The photocatalytic activity of the resulting samples was investigated by oxidation of NO at ppb levels in a continuous flow reactor at ambient temperature. The volume of the rectangular reactor, which was made of stainless steel and covered with Saint-Glass, was 4.5 L (30 cm ×15 cm×10 cm). A 150 W commercial tungsten halogen lamp was vertically placed outside the reactor above the reactor. Adequate distance was also kept from the lamp to the reactor for the same purpose to keep the temperature at a constant level. For the visible light photocatalytic activity test, UV cutoff filter (420 nm) was adopted to remove UV light. For each photocatalytic activity test experiment, two sample dishes (with a diameter of 12 cm) containing the photocatalyst powders was placed in the center of the reactor. The photocatalyst samples were prepared by coating an aqueous suspension of the samples onto the glass dish and then dried at 60 ^{o}C. The weight of the photocatalysts used for each dish was kept at 0.10 g. The NO gas was acquired from a compressed gas cylinder at a concentration of 100 ppm of NO (N_2 balance). The initial concentration of NO was diluted to 550 ppb by the air stream supplied by purified air. The desired relative humidity (RH) level of the NO flow was controlled at 60% by passing the zero air streams through a humidification chamber. The gas streams were premixed completely by a gas blender, and the flow rate was controlled at 3.3 L/min by a mass flow controller. After the adsorption–desorption equilibrium was achieved, the lamp was turned on. The concentration of NOx was continuously measured by a chemiluminescence NOx analyzer (Thermo Environmental Instruments Inc., 42i-TL), which monitors NO, NO_2, and NOx (NOx represents $NO+NO_2$) with a sampling rate of 1.0 L/min. The NO removal ratio (η) was calculated as $\eta(\%) = (1–C/C_0) \times 100\%$, where C and C_0 are concentrations of NO in the outlet steam and the feeding stream, respectively.
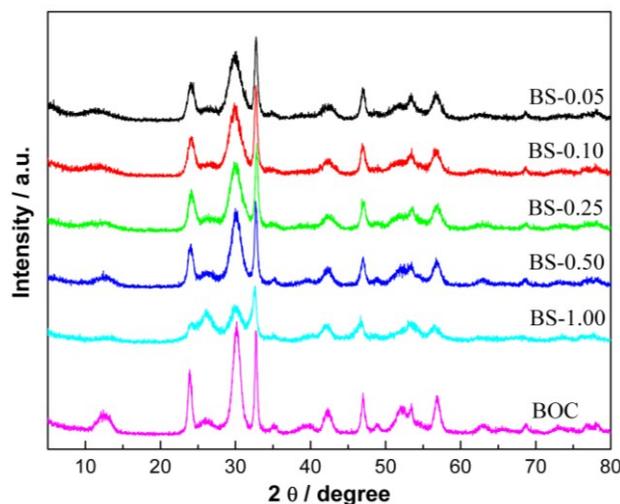
3. Results and discussion

Fig. 1 XRD patterns of as-prepared BOC and $(BiO)_2CO_3$/amorphous Bi_2S_3 heterostructures.

3.1 Phase structure

The solubility of Bi_2S_3 is much lower than that of $(BiO)_2CO_3$. Thus, with the presence of S^{2-} ions, part of $(BiO)_2CO_3$ could transform into Bi_2S_3 rapidly, resulting in the formation of $(BiO)_2CO_3$/amorphous Bi_2S_3 composites. Fig. 1 presents the XRD patterns of pure $(BiO)_2CO_3$ and $(BiO)_2CO_3/Bi_2S_3$ with different Bi_2S_3 contents. The diffraction peaks of all the samples are sharp and intense. All the peaks detected can be indexed to $(BiO)_2CO_3$ (JCPDS-ICDD Card No.41-1488). No peaks of any other phases or impurities can be observed. The intensity of diffraction peaks of $(BiO)_2CO_3$/amorphous Bi_2S_3 samples is gradually decreased as the content of Bi_2S_3 is increased. However, from the XRD patterns, no significant peaks of Bi_2S_3 can be detected, which indicates that Bi_2S_3 is amorphous. As the Bi_2S_3 component is amorphous and exhibits no diffraction peaks, the inclusion of amorphous Bi_2S_3 into the composites would result in lowered diffraction intensity. When the content of amorphous Bi_2S_3 is increased, the diffraction peaks of the composites samples would be decreased. By hydrothermal treatment of the anion-exchange process, the $(BiO)_2CO_3$/crystalline Bi_2S_3 can be obtained (Fig. S1). This fact further

3

suggests the presence of amorphous Bi_2S_3 on the surface of $(BiO)_2CO_3$ under ambient anion-exchange process.

3.2 Chemical composition

In order to confirm the chemical state of the elements in the sample, XPS were carried out. Fig. 2a shows the wide-scan XPS spectra of BS-0.25, in which Bi, S, O and C elements can be observed. In Fig. 2b, we can see two strong peaks at 164.1 and 158.8 eV that are corresponded to Bi $4f_{5/2}$ and Bi $4f_{7/2}$ of Bi^{3+} in the sample. The peak at 160.9 eV can be assigned to the binding energy of the S2p orbital in the form of S^{2-}, which also indicates the formation of Bi_2S_3.[12] Fig. 2c shows the XPS spectra for C1s, where the peaks centered at 284.8, 286.3, 287.6, and 288.7 eV can be attributed to C–C, C–O, C=O and O=C–O groups, respectively.[46-47] The O1s spectra (Fig. 2d) are also recorded, which can be fitted by three peaks at binding energies of 529.7, 530.9 and 532.4 eV, respectively. The peak at 530.9 eV is characteristic of Bi–O binding energy in $(BiO)_2CO_3$, and the other two peaks at 529.7 and 532.4 eV can be assigned to carbonate species and adsorbed H_2O on the surface.[32] From the XPS spectra, it can be concluded that the heterostructure consist of $(BiO)_2CO_3$ and Bi_2S_3 with no other residual impurities.
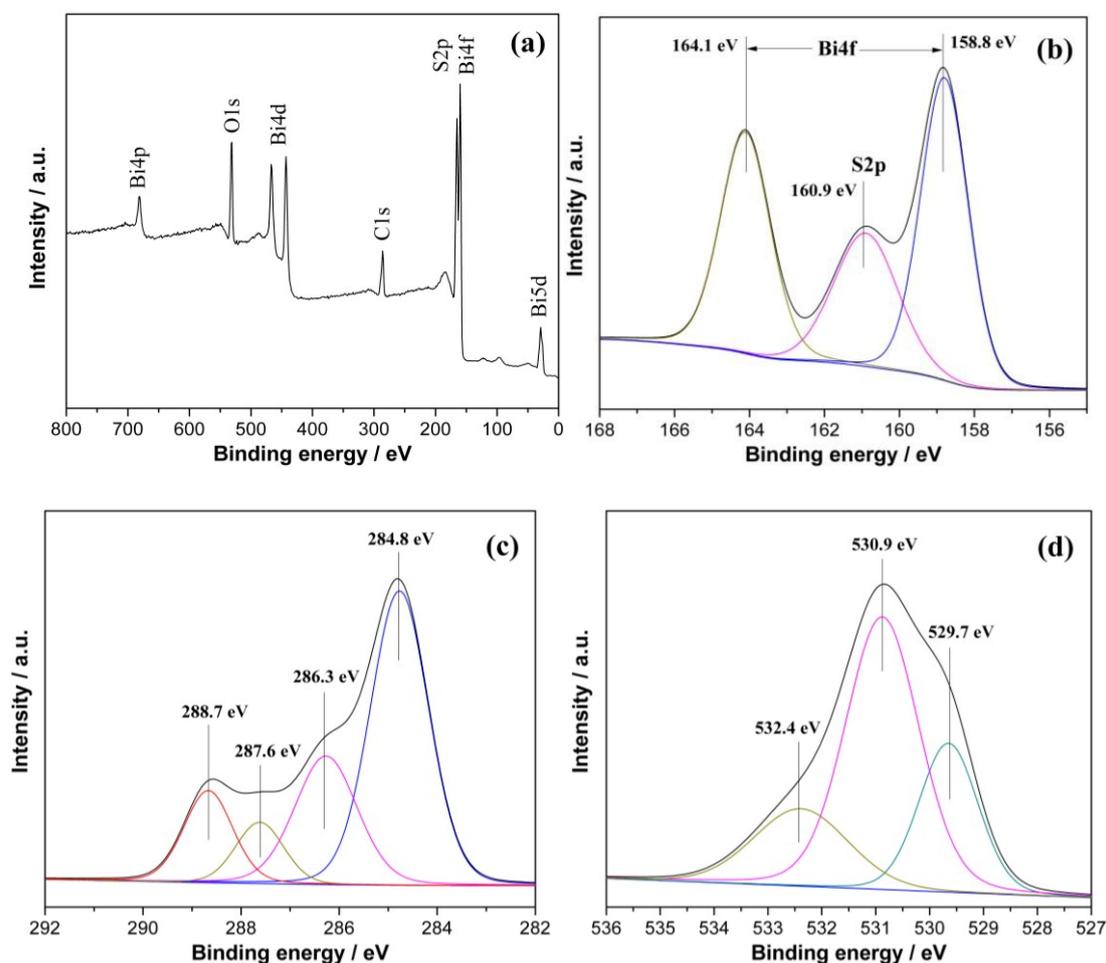

Fig. 2 XPS spectra of BS-0.25, survey (a), Bi4f and S2p (b), C1s (c) and O1s (d).

FT-IR spectra of $(BiO)_2CO_3$ and $(BiO)_2CO_3$/amorphous Bi_2S_3 samples are shown in Fig. 3. The two peaks at 3389 and 1730 cm^{-1} can be attributed to the stretching and deformation vibrations of the O-H groups of the chemisorbed and/or physisorbed water molecules. Four characteristic band groups of CO_3^{2-} at 1067 cm^{-1} (symmetric stretching mode ν_1), 846 and 820 cm^{-1} (out-of plane bending mode ν_2), 1468 and 1391 cm^{-1} (antisymmetric vibration ν_3), 670 cm^{-1} (in-plane deformation ν_4), and 1756 and 1730 cm^{-1} ($\nu_1 + \nu_4$) are observed for all the samples.[48] The peak at 2373 cm^{-1} derived from the vibration of the CO_3^{2-} is also observed. The peaks at 1382 and 1103 cm^{-1} can be assigned to the Bi–S bond vibrations arising from amorphous Bi_2S_3.[12] The peak at 1382 cm^{-1} is overlapped with the peak of CO_3^{2-} (1391 cm^{-1}), so the change of this peak cannot be observed directly. Further observation of the peak at 1103 cm^{-1} indicates that the intensity of this peak is slightly increased with the increased amount of Bi_2S_3.
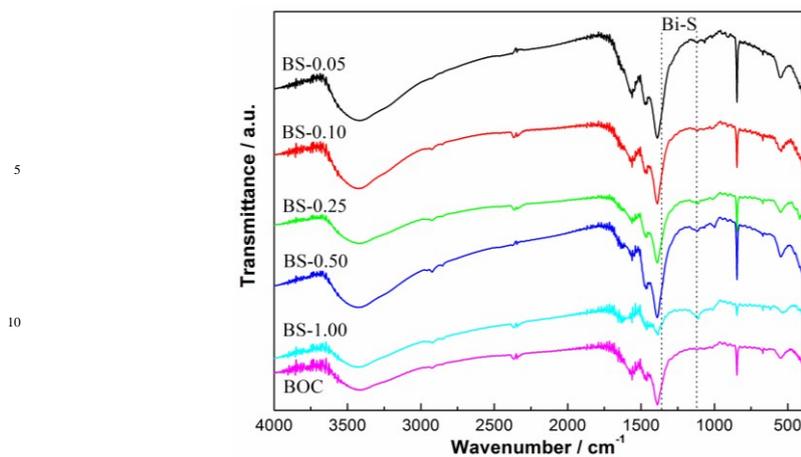
4

Fig. 3 FT-IR spectra of the as-prepared BOC and $(BiO)_2CO_3$/amorphous Bi_2S_3 heterostructures.

3.3 Morphological structure.

Fig. 4a and 4b shows the SEM images of pure $(BiO)_2CO_3$ sample, which consists of many three-dimensional (3D) flower-like hierarchical microspheres self-assembled by two-dimensional (2D) interleaved nanosheets.[32] The sizes of the microspheres range from 0.7 to 1.3 μm. After reacting with Na_2S, the morphology of $(BiO)_2CO_3$ has not changed obviously (Fig. 5a, 5b, 5c and 5d). Further observation in Fig. 5c and 5d shows that there are some particles deposited uniformly on the surface of the nanosheets. These particles should be amorphous Bi_2S_3. The EDX maps (Fig. 5e, 5f, 5g and 5h) indicate the elemental distribution of C, O, Bi and S. Obviously, amorphous Bi_2S_3 are homogeneously distributed on the surface of the $(BiO)_2CO_3$/Bi_2S_3 heterostructures. The TEM images (Fig. 6a and 6b) shows the microsphere morphology of BS-0.25. Fig. 6c shows the local region of one microsphere and some particles can be observed on the surface. From the HRTEM image (Fig. 6d), the lattice spacing of 0.292 nm can be well assigned to the (013) plane of $(BiO)_2CO_3$. The lattice of Bi_2S_3 cannot be observed as Bi_2S_3 is amorphous, which is consistent with XRD. The amorphous Bi_2S_3 is attached on the surface (Fig. 6d), indicating the anion-exchange reaction takes place on the surface of the nanosheets. The generation of amorphous Bi_2S_3 results in the formation of $(BiO)_2CO_3$/amorphous Bi_2S_3 heterostructure.[43]
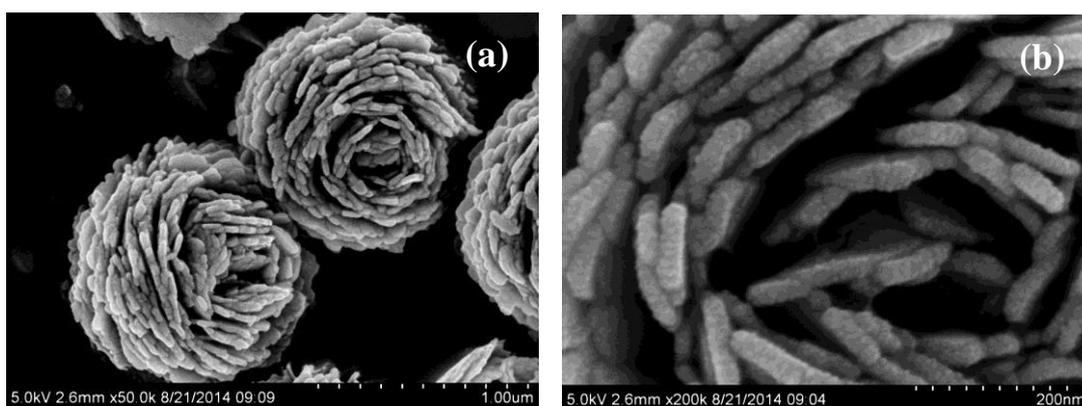

Fig. 4 SEM images (a, b) of BOC.

5

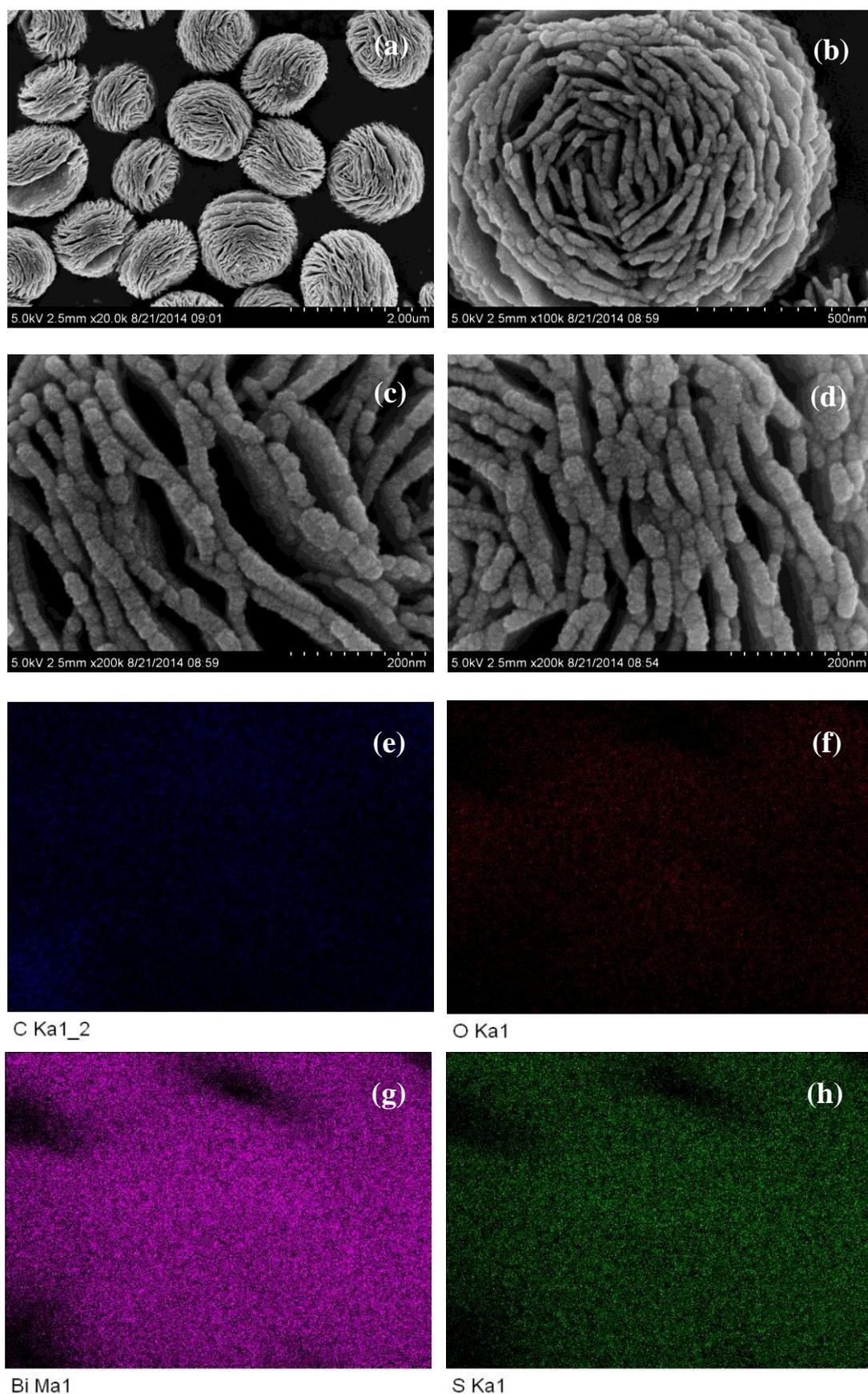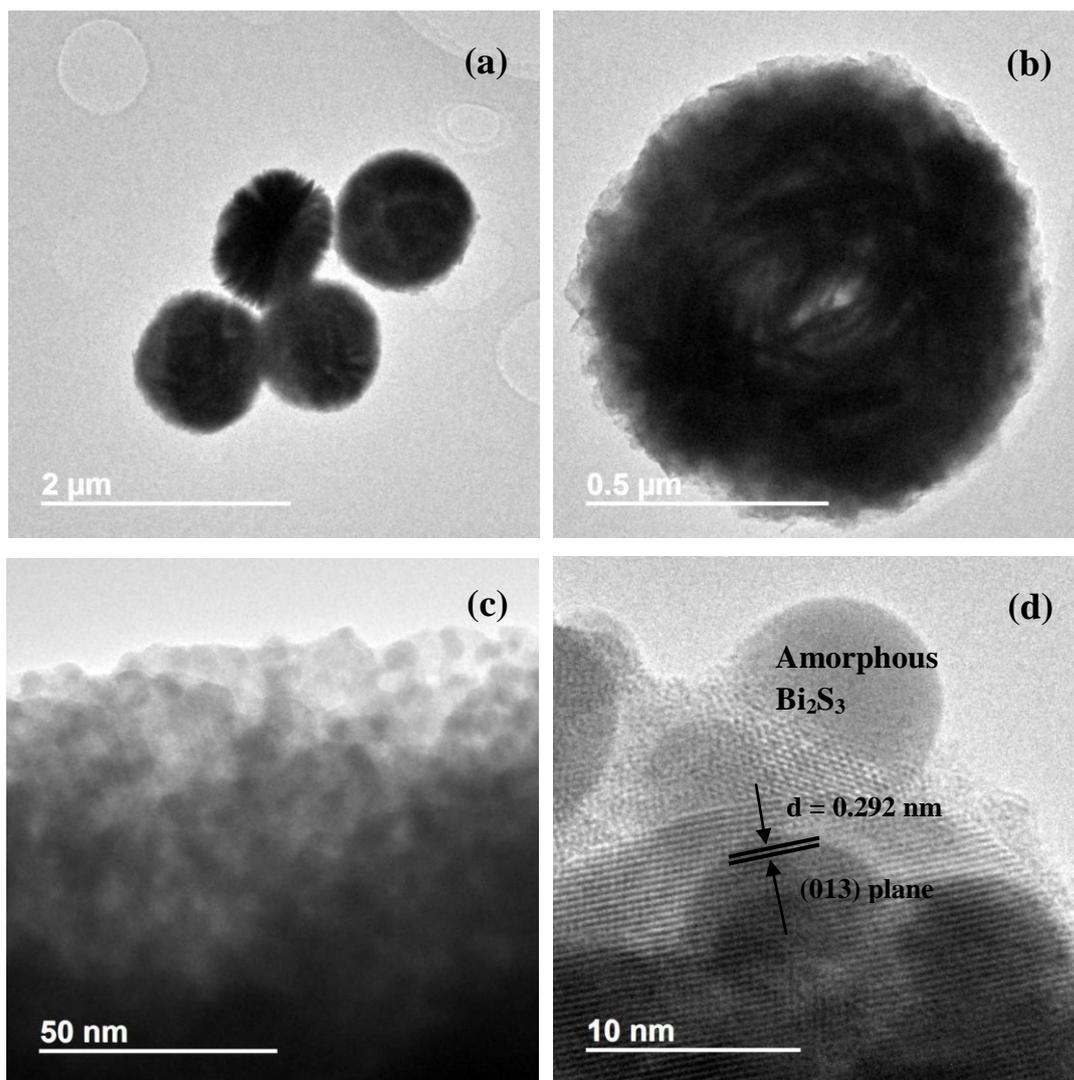**Fig. 5** SEM images (a, b, c, d) and EDX mapping (e, f, g, h) of BS-0.25.
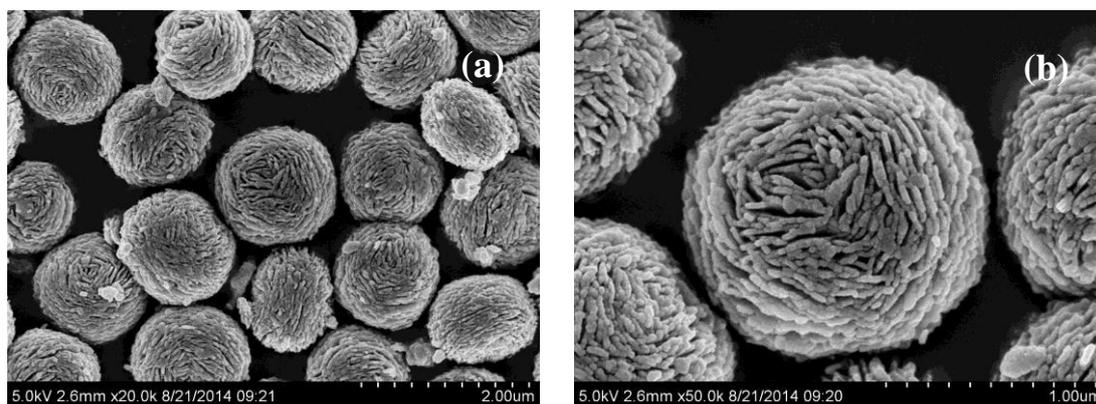
5

6

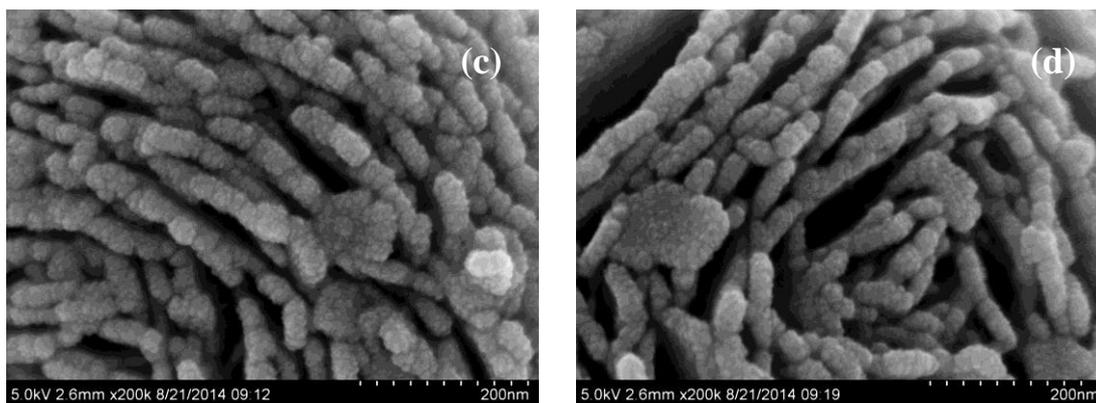**Fig. 6** TEM (a,b, c) and HRTEM (d) images of BS-0.25.

5

20

25

Fig. 7 SEM images (a, b, c, d) of BS-1.00.

Fig. 7 shows the SEM images of BS-1.00. When the amount of Na_2S is increased to 50%, more Bi_2S_3 particles will be produced. The microsphere morphology does not change, however, some large particles are attached on the surface (Fig. 7a and 7b), which can be ascribed to the aggregation of small Bi_2S_3 nanoparticles. The increased content of amorphous Bi_2S_3 on the surface of $(BiO)_2CO_3$ microspheres leads to the decreased peak intensity in the XRD pattern (Fig. 1). The formation process of 3D $(BiO)_2CO_3$/amorphous Bi_2S_3 heterostructured hierarchical microspheres by anion exchange process is shown in Scheme 1.

$$(BiO)_2CO_3 + 3Na_2S + 2H_2O \longrightarrow Bi_2S_3 + Na_2CO_3 + 4NaOH$$
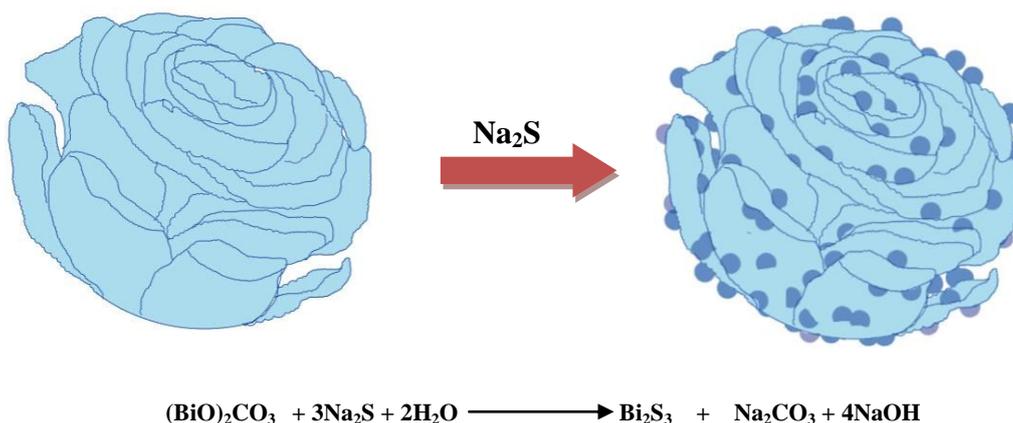
Scheme 1 Formation of 3D $(BiO)_2CO_3$/amorphous Bi_2S_3 heterostructured hierarchical microspheres by a controllable anion exchange process.

Nitrogen adsorption-desorption measurement was used to study the Brunauer–Emmett–Teller (BET) surface areas and the corresponding pore size distribution of pure $(BiO)_2CO_3$ and $(BiO)_2CO_3$/amorphous Bi_2S_3 heterosructures. According to the Brunauer-Deming-Deming-Teller (BDDT) classification, the majority of physisorption isotherms can be classified into six types. As showed in Fig. 8a, all the samples have an isotherm of type IV, which indicates the presence of mesopores. Comparing with BOC, the heterostructured samples display a higher absorption at the relatively high pressure, indicating the presence of more mesopores.[49-50] The surface areas and pore volumes of all the samples are shown in Table 1. The slightly increased surface areas and pore volumes of heterostructured samples is associated with the formation of amorphous Bi_2S_3 on the surface. Furthermore, the shape of the hysteresis loops is of type H3, implying the existence of slit-like pores, which is consistent with the TEM observations. The corresponding pore size distribution (PSD) curves of the samples are shown in Fig. 8b. The PSD curves range from 2 to 100 nm and is bimodal with small mesopores (3.2~2.7 nm) and larger ones (7.2~10.8 nm). The small mesopores can be ascribed to the pores formed among the aggregated BOC nanosheets and Bi_2S_3 nanoparticles, and the large mesopores are ascribed to the pores formed between the stacked microspheres.[32]
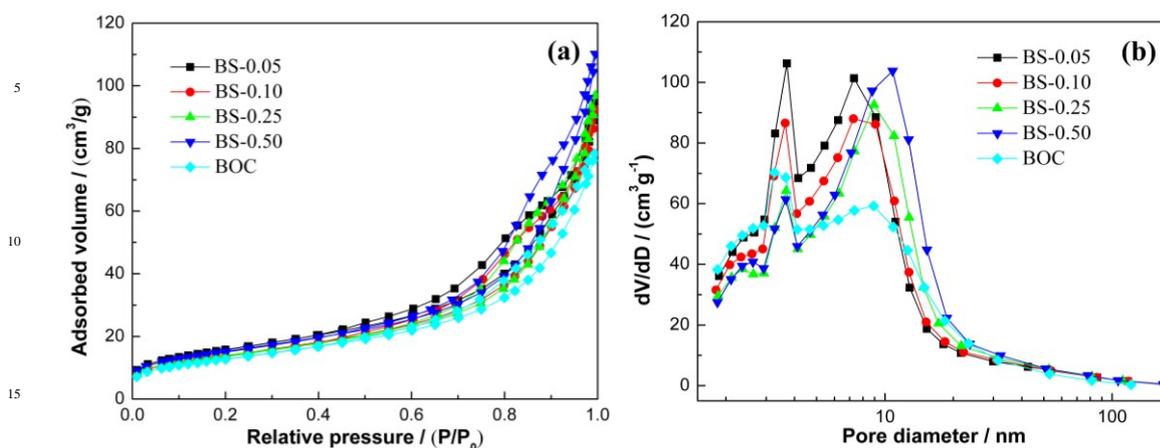
8

Fig. 8 N_2 adsorption-desorption isotherms (a) and pore size-distribution curves (b) of BOC and (BiO)$_2$CO$_3$/amorphous Bi$_2$S$_3$ heterosructures.

Table 1 The S_{BET}, pore volume, peak pore diameter, NO removal ratio of the samples.

Sample name	S_{BET} (m^2/g)	Pore volume (cm^3/g)	Peak pore diameter (nm)	NO η (%)
BOC	46	0.122	3.2/8.9	21.5
BS-0.05	56	0.147	3.7/7.2	48.6
BS-0.10	50	0.143	3.6/7.3	51.4
BS-0.25	49	0.150	3.6/9.0	57.1
BS-0.50	54	0.171	3.7/10.8	45.1

3.4 Optical property and band structure.

The pure BOC and (BiO)$_2$CO$_3$/amorphous Bi$_2$S$_3$ heterosructures with the increasing of molar ratio of Bi$_2$S$_3$ show a gradient color deepening from white to black. From the UV-vis absorption spectra (Fig. 9), we can see that the pure BOC displayed the absorption edge around 370 nm. With the increasing molar ratio of Bi$_2$S$_3$ from 0.05 to 1.00, the light absorption spectra of the heterostructured samples are broadened dramatically from UV to the whole visible light region. This interesting observation can be owing to the special properties of Bi$_2$S$_3$ with small band gap, large absorption coefficient and strong absorption in nearly all the visible light range. The increased solar absorption is beneficial for enhancement of photocatalytic activity.
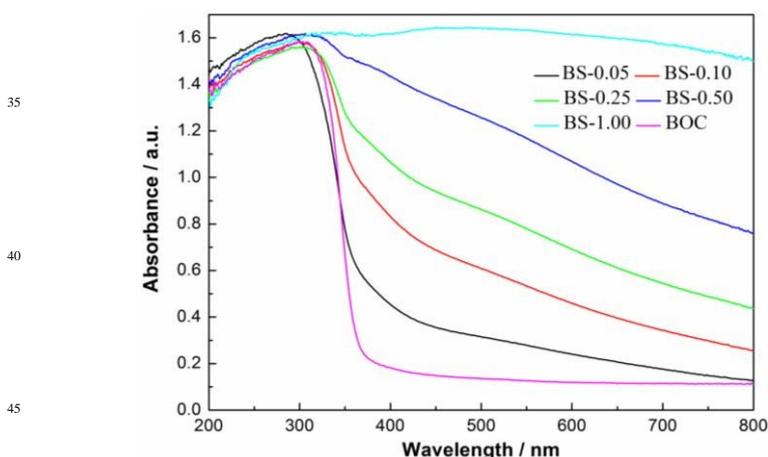

Fig. 9 UV-vis DRS spectra of BOC and (BiO)$_2$CO$_3$/amorphous Bi$_2$S$_3$ samples.

9

The band-edge positions of the semiconductors in the heterostructures have a pivotal influence on charge separation and transfer. The valence band (VB) edge of a semiconductor at the point of zero charge can be calculated by the empirical equation $E_{VB} = X - E^e + 0.5Eg$, where E_{VB} is the valence band-edge potential, X is the electronegativity of the semiconductor expressed as the geometric mean of the absolute electronegativity of the constituent atoms, E^e is the energy of free electrons on the hydrogen scale (about 4.5 eV), and Eg is the band-gap energy of the semiconductor.[51-52] The conduction band (CB) edge E_{CB} can be determined by $E_{CB} = E_{VB} - Eg$. The X values for $(BiO)_2CO_3$ and Bi_2S_3 are 6.36 and 5.27eV, respectively. The band-gap energies of $(BiO)_2CO_3$ and Bi_2S_3 is 3.33 and 1.3 eV. From the equation above, the top of VB and the bottom of CB of $(BiO)_2CO_3$ and Bi_2S_3 can be calculated 0.20 and 3.53 eV for $(BiO)_2CO_3$; 0.12 and 1.41eV for Bi_2S_3. The energy band levels of $(BiO)_2CO_3/Bi_2S_3$ heterostructures and the possible charge separation process are proposed in Scheme 1. Under visible light irradiation, Bi_2S_3 can be easily excited and electrons and holes are generated. For $(BiO)_2CO_3$ microspheres (SEM in Fig. 4), the special hierarchical structure could induce effects of multiple light surface scattering and reflecting (SSR effect) and increase the effective optical path-length of a photon and absorption probability.[32] Thus, the electrons and holes pairs can also be produced for $(BiO)_2CO_3$ via the SSR effect.[32] As the CB of Bi_2S_3 is more negative than that of $(BiO)_2CO_3$, the electrons on the CB of Bi_2S_3 can transfer to the CB of $(BiO)_2CO_3$ easily. As the CB of $(BiO)_2CO_3$ is more positive than that of Bi_2S_3, holes in $(BiO)_2CO_3$ will be migrated to the VB of Bi_2S_3. In this way, the photoinduced electrons and holes can be separated efficiently over the $(BiO)_2CO_3$/amorphous Bi_2S_3 heterostructures.
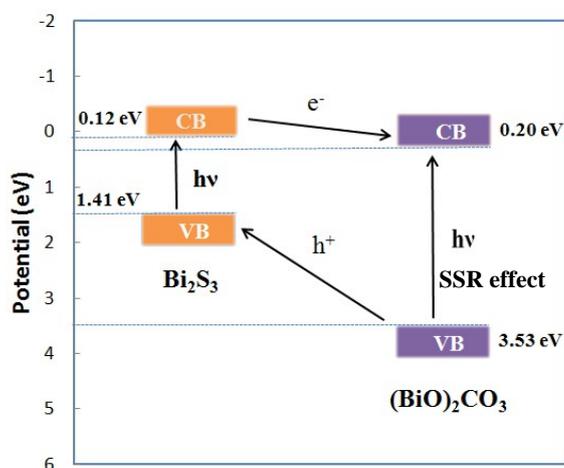
Scheme 2 Diagram for energy band levels of $(BiO)_2CO_3$/amorphous Bi_2S_3 composites and the possible charge separation process.

PL spectra are widely used to survey the recombination rate of the photogenerated electron-hole pairs. The decrease in the recombination rate gives rise to a low PL intensity. Fig. 10 shoes the PL emission spectra of BOC and $(BiO)_2CO_3$/amorphous Bi_2S_3 heterostructures at room temperature. The pure BOC shows a strong emission peak. After hybridization with amorphous Bi_2S_3, the PL intensity is greatly decreased. The PL intensity is decreased with the increased content of Bi_2S_3. The result implies that the combination of $(BiO)_2CO_3$ and Bi_2S_3 is powerful way to separate photogenerated electron–hole pairs.
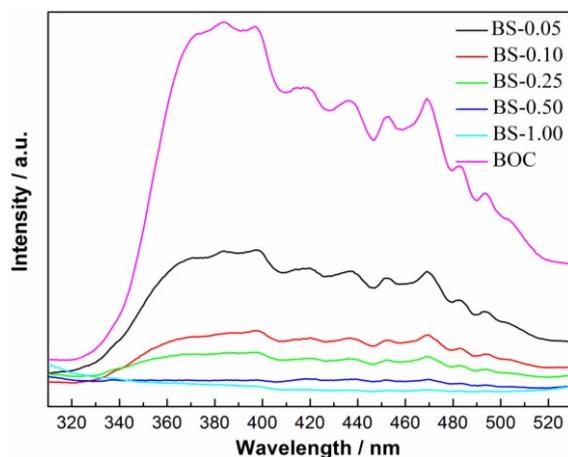

Fig. 10 PL emission spectra of pure BOC and $(BiO)_2CO_3$/amorphous Bi_2S_3 heterostructures excited at 280nm at

10

room temperature.

3.5 Photocatalytic activity and stability.

The as-prepared samples were used to photocatalytic removal of ppb-level NO in gas phase in order to demonstrate their potential capability for air purification. Fig. 11a shows the variation of NO concentration (C/C$_0$%) with irradiation time under visible light irradiation. NO could not be photolyzed under light irradiation (λ> 420 nm). Pure BOC shows NO removal ratio of 21 % under visible light irradiation through SSR effect. When amorphous Bi$_2$S$_3$ is introduced, the resulted (BiO)$_2$CO$_3$/amorphous Bi$_2$S$_3$ heterostructures exhibit highly enhanced activity. Under optimized condition, BS-0.25 sample shows the most efficient activity with a NO removal ratio of 57.1%, which is even higher than that of N-doped (BiO)$_2$CO$_3$,[29-30,33] BiOX [53,54] and C$_3$N$_4$ [55,56] under similar test conditions. When the molar ratio of Bi$_2$S$_3$ to (BiO)$_2$CO$_3$ is increased to 1.00, excessive amounts of Bi$_2$S$_3$ particles would cover all the surface of (BiO)$_2$CO$_3$. As a result, the BS-1.00 sample looses the activity. As all the samples have similar surface areas and morphology, the highly enhanced photocatalytic performance of (BiO)$_2$CO$_3$/Bi$_2$S$_3$ (BS-0.25) can be attributed to the heterostructures that effectively promote the separation of charge carriers and increase solar absorption that promotes the utilization of visible light. As the charge separation is promoted and the visible light utilization is broadened, more charges will take part in the photocatalytic reaction and more radicals will be produced. This could explain the inhibited NO$_2$ generation during reaction (Fig. 11b), which is also beneficial for application as NO$_2$ is more toxic. For the (BiO)$_2$CO$_3$/crystalline Bi$_2$S$_3$, the photocatalytic activity of is actually decreased, which indicates the siginificant advantages of (BiO)$_2$CO$_3$/amorphous Bi$_2$S$_3$.
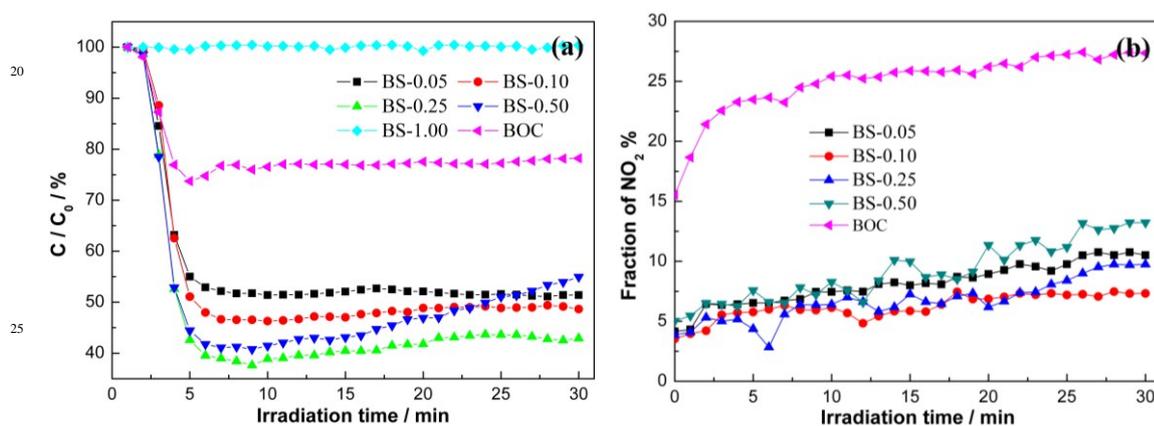

Fig. 11 Visible light photocatalytic activity of pure BOC and (BiO)$_2$CO$_3$/amorphous Bi$_2$S$_3$ composites for NO removal.(a) and evolution of NO$_2$ in the outlet (b).
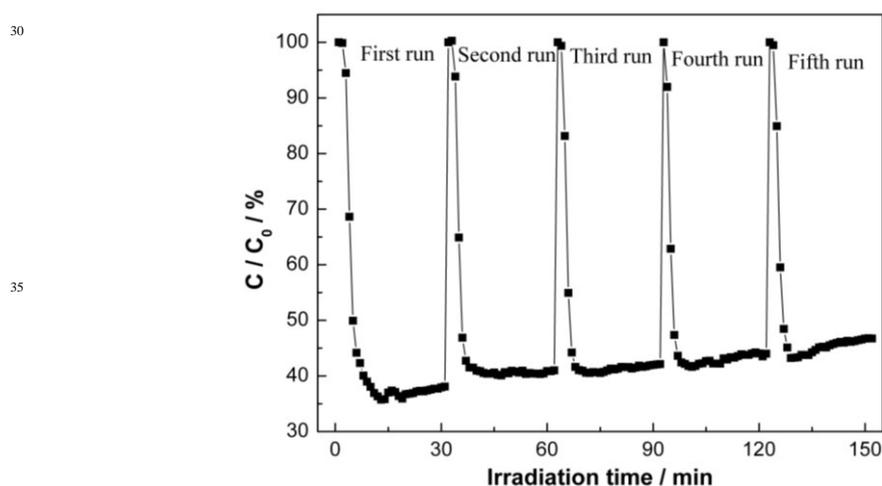

Fig. 12 The repeated visible light photocatalytic activities of BS-0.25 for the removal of NO in air.

The photochemical stability of a photocatalyst under repeated irradiation should be considered for practical applications. An excellent photocatalyst should maintain stable activity so that the catalyst can be used repeatedly. To test the stability, we conduct multiple runs of photocatalytic reaction for NO$_x$ removal. It can be seen from Fig.

11

12 that BS-0.25 exhibit an excellent stability in activity without deactivation under repeated irradiations.

4. Conclusion

In summary, we have synthesized 3D hierarchical $(BiO)_2CO_3/Bi_2S_3$ heterostructures by a facile anion-exchange method. Compared to others, our Bi_2S_3 was formed on the surface of $(BiO)_2CO_3$ hierarchical microspheres in amorphous form. The heterostructured photocatalysts exhibited drastically enhanced visible light photocatalytic activity and promoted oxidation of NO. The BS-0.25 has the maximal photocatalytic efficiency with a removal ratio of 57.1%, which is much higher than other types of photocatalyst. The combination of $(BiO)_2CO_3$ and amorphous Bi_2S_3 could extend the spectral responsive range of $(BiO)_2CO_3$ microspheres and promote the transfer of photogenerated carriers, leading to enhanced photocatalytic activities. This finding can be extended that the $(BiO)_2CO_3$ hierarchical microspheres are used as the substrate precursor and the structural template to combine with other components by ion exchange strategy. The present work could also open up a new avenue for construction of heterostructures by amorphous components.

Acknowledgements

References

1 Z. F. Huang, L. Pan, J. Zhou, X. W. Zhang and Li Wang, *Nanoscale*, 2014, **6**, 14044.

2 L. S. Zhang, H. L. Wang, Z. G. Chen, P. K. Wong and J. S. Liu, *Appl. Catal. B.*, 2011, **106**, 1.

3 N. Zhang, R. Ciriminna, M. Pagliaro and Y. J. Xu, *Chem. Soc. Rev.*, 2014, **43**, 5276.

4 X. B. Cao, Z. F. Lu, L. W. Zhu, L. Yang, L. Gu, L. L. Cai and J. Chen, *Nanoscale*, 2014, **6**, 1434.

5 L.W. Zhang and Y. F. Zhu, *Catal. Sci. Technol.*, 2012, **2**, 694.

6 S. M. Sun and W. Z. Wang. *RSC Adv.*, 2014, **4**, 47136.

7 J. Li, Y. Yu and L. Z. Zhang, *Nanoscale*, 2014, **6**, 8473.

8 H. F. Cheng, B. B. Huang and Y. Dai, *Nanoscale*, 2014, **6**, 2009.

9 X. H. Gao, H. B. Wu, L. X. Zheng, Y. J. Zhong, Y. Hu and X. W. Lou. *Angew. Chem. Int. Ed.*, 2014, **53**, 1.

10 H. F. Cheng, B. B. Huang, X. Y. Qin, X. Y. Zhang and Y. Dai, *Chem. Commun.*, 2012, **48**, 97.

11 D. K. Ma, M. L. Guan, S. S. Liu, Y. Q. Zhang, C. W. Zhang, Y. X. He and S. M. Huang, *Dalton Trans.*, 2012, **41**, 5581.

12 J. Cao, B. Y. Xu, H. L. Lin, B. D. Luo and S. F. Chen, *Dalton Trans.*, 2012, **41**, 11482.

13 L. Chen, S. F. Yin, S. L. Luo, R. Huang, Q. Zhang, T. Hong and P. C. T. Au, *Ind. Eng. Chem. Res.*, 2012, **51**, 6760.

14 F. Dong , Y. J. Sun, M. Fu, Z. B. Wu and S.C. Lee, *J. Hazard. Mater.*, 2012, **219**, 26.

15 D. Yue, D. Chen, Z. Wang, H. Ding, R. Zong, and Y. F. Zhu, *Phys. Chem. Chem. Phys.*, 2014, **16**, 26314.

16 C. Zhang and Y. F. Zhu, *Chem. Mater.*, 2005, **17**, 3537.

17 L.W. Zhang, T.G. Xu, X. Zhao and Y. F. Zhu, *Appl. Catal. B*, 2010, **98**, 138.

18 J. Yu and A. Kudo, *Adv. Funct. Mater.*, 2006, **16**, 2163.

19 X. Zhang, Z. H. Ai, F. L. Jia and L. Z. Zhang, *J. Phys. Chem. C*, 2008, **112**, 747.

20 Y. N. Huo, M. Miao, Y. Zhang, J. Zhu and H. X. Li, *Chem. Commun.*, 2011, **47**, 2089.

21 Z. F. Bian, Y. N. Huo, Y. Zhang, J. Zhu and Y. F. Lu, *Appl. Catal. B*, 2009, **91**, 247.

22 J. J. Wu, F. Q. Huang, X. J. Lü, P. Chen, D. Y. Wan and F. F. Xu, *J. Mater. Chem.*, 2011, **21**, 3872.

23 Y. S. Xu and W. D. Zhang, *Appl. Catal. B*, 2013, **140**, 306.

24 L. Q. Ye, Y. R. Su, X. L. Jin, H. Q. Xie and C. Zhang, *Environ. Sci.: Nano*, 2014, **1**, 90.

25 S. J. Peng, L. L. Li, H. T. Tan, Y. Z. Wu, R. Cai, H. Yu, X. Huang, P. N. Zhu, S. Ramakrishna, M. Srinivasan and Q. Y. Yan, *J. Mater. Chem. A*, 2013, **1**, 7630.

26 P. Madhusudan, J. G. Yu, W. G. Wang, B. Cheng and G. Liu, *Dalton Trans.*, 2012, **41**, 14345.

27 Y. L. Zhang, D. Y. Li, Y. G. Zhang, X. F. Zhou, S. J. Guo and L. B. Yang, *J. Mater. Chem. A*, 2014, **2**, 8273.

28 F. Dong, A. M. Zheng, Y. J. Sun, M. Fu, B. Q. Jiang, W. K. Ho, S. C. Lee and Z. B. Wu, *CrystEngComm*, 2012, **14**, 3534.

29 T. Xiong, F. Dong and Z. B. Wu, *RSC Advances*, 2014, **4**, 56307.

30 F. Dong, H. T. Liu, W. K. Ho, M. Fu and Z. B. Wu, *Chem. Eng. J.*, 2013, **214**, 198

31 Y. Y. Liu, Z. Y. Wang, B. B. Huang, K. S. Yang, X. Y. Zhang, X. Y. Qin and Y. Dai, *Appl. Surf. Sci.*, 2010, **257**, 172.

32 F. Dong, Q. Y. Li, Y. Zhou, Y. J. Sun, H. D. Zhang and Z. B. Wu, *Dalton Trans.*, 2014, **43**, 9468.

33 F. Dong, T. Xiong, R. Wang, Y. J. Sun and Y. K. Jiang, *Dalton Trans.*, 2014, **43**, 6631.

12

34 W. D. Zhang, Y. J. Sun, F. Dong, W. Zhang, S. Duan and Q. Zhang, *Dalton Trans.*, 2014, **43**, 12026.

35 L. Ma, W. Hu, Q. L. Zhang, P. Y. Ren, X. J. Zhuang, H. Zhou, J. Y. Xu, H. L. Li, Z. P. Shan, X. X. Wang, L. Liao, H. Q. Xu and A. L. Pan, *Nano Lett.*, 2014, **14**, 694.

36 S. J. Hong, S. Lee, J. S. Jang and J. S. Lee, *Energy Environ. Sci.*, 2011, **4**, 1781.

37 X. F. Zhang, Y. Gong, X. L. Dong, X. X. Zhang, C. Ma and F. Shi, *Mater. Chem. Phys.*, 2012, **136**, 472.

38 S. Balachandran and M. Swaminathan, *Dalton Trans.*, 2013, **42**, 5338.

39 S. C. Liufu, L. D. Chen, Q. Yao and C. F. Wang, *Appl. Phys. Lett.*, 2007, **90**, 112106.

40 G. Konstantatos, L. Levina, J. Tang and E. H. Sargen, *Nano Lett.*, 2008, **8**, 4002.

41 O. Rabin, J. M. Perez, J. Grimm, G. Wojtkiewicz and R. Weissleder, *Nat. Mater.*, 2006, **5**, 118.

42 L. S. Li, N. J. Sun, Y. Y. Huang, Y. Qin, N. N Zhao, J. N. Gao, M. X. Li, H. H. Zhou and L. M. Qi, *Adv. Funct. Mater.*, 2008, **18**, 1194.

43 N. Liang, J. T. Zai, M. Xu, Q. Zhu, X. Wei and X. F. Qian, *J. Mater. Chem. A*, 2014, **2**, 4208.

44 X. F. Cao, L. Zhang, X. T. Chen and Z. L. Xue. *CrystEngComm*, 2011, **13**, 1939.

45 W. J. Wang, H. F. Cheng, B. B. Huang, X. J. Lin, X. Y. Qin, X. Y. Zhang and Y. Dai, *J. Colloid Interface Sci.*, 2013, **6**, 34.

46 G. P. Dai, S. Q. Liu, Y. Liang and K. Liu, *RSC Adv.*, 2014, **4**, 34226.

47 H. Xu, Y. X. Song, Y. H. Song, J. X. Zhu, T. T. Zhu, C. B. Liu, D. X. Zhao, Q. Zhang and H. M. Li, *RSC Adv.*, 2014, **4**, 34539.

48 G. E. Tobon-Zapata, S. B. Etcheverry and E. J. Baran, *J. Mater. Sci. Lett.*, 1997, **16**, 656.

49 H. Q. Jiang, M. Nagai and K. Kobayashi, *J. Alloys Compd.*, 2009, **479**, 821 .

50 H. Xu, H. M. Li, C. D. Wu, J. Y. Chu, Y. S. Yan, H. M. Shu and Z. Gu, *J. Hazard. Mater.*, 2008, **153**, 877.

51 M. C. Long, W. M. Cai, B. X. Zhou, X. Y. Chai and Y. H. Wu, *J. Phys. Chem. B*, 2006, **110**, 20211.

52 M. A. Bulter and D. S. Ginley, *J. Electrochem. Soc.*, 1978, **125**, 228.

53 W. D. Zhang, Q. Zhang and F. Dong, *Ind. Eng. Chem. Res.*, 2013, **52**, 6740.

54 Y. J. Sun, W. D. Zhang, T. Xiong, Z. W. Zhao, F. Dong, R. Q. Wang and W. K. Ho, *J. Colloid Interface Sci.*, 2014, **418**, 317.

55 F. Dong, M. Y. Ou, Y. K. Jiang, S. Guo, Z. B. Wu, *Ind. Eng. Chem. Res.*, 2014, **53**, 2318.

56 F. Dong, Z. Y. Wang, Y. J. Sun, W. K. Ho and H. D. Zhang, *J. Colloid Interface Sci.*, 2013, **401**, 70.